First Nonhuman Primate-Sized Magnetic Particle Imaging System Based on Digital-Scanned Focus Field

Zechen Wei, Yanjun Liu, Sijia Liu, Xiaomei Yu, Haoran Zhang, Tao Zhu, Bo Zhang, Yali Zhang, Hongdi Huang, Yang Fan, Hongli Li, Jianhong Wang, Jie Tian, *Fellow, IEEE*, and Hui Hui, *Member, IEEE*

***Abstract*— Magnetic particle imaging (MPI) is a burgeoning imaging modality that facilitates the reconstruction of position and concentration of superparamagnetic iron oxide nanoparticles. Its potential in clinical applications is substantial, leading to an increasing demand for larger bore sizes in MPI systems. However, the challenge lies in maintaining high resolution, sensitivity, and real-time imaging advantages in larger systems. In this article, we present the design of a 3-D MPI system tailored for nonhuman primates (NHP-MPI) with a bore size of 190 mm. The application of a 3-D digital-scanned focus field is applied to obtain highly sensitive imaging, and the system operates cooling-free under low gradient conditions. In imaging experiments involving a macaque's brain, our system demonstrated good quantitative performance. The 3-D MPI image yielded satisfactory results for fusion with other structural imaging modalities.**

***Index Terms*— Digital scanned, focus field, magnetic particle imaging (MPI), nonhuman primate (NHP).**

Manuscript received 19 January 2024; revised 15 April 2024; accepted 30 April 2024. Date of publication 24 June 2024; date of current version 3 July 2024. This work was supported in part by the National Key Research and Development Program of China under Grant 2021YFF0702700; in part by the National Natural Science Foundation of China under Grant 62027901, Grant 92359304, Grant U23A6011, Grant 81930053, and Grant 81227901; in part by Beijing Natural Science Foundation under Grant JQ22023; in part by Chinese Academy of Sciences (CAS) Youth Innovation Promotion Association under Grant Y2022055; in part by the STI2030-Major Projects under Grant 2021ZD0203900 and Grant 2022ZD0205100; and in part by Yunnan Province under Grant 202305AH340006. The Associate Editor coordinating the review process was Dr. Yandan Jiang. *(Zechen Wei, Yanjun Liu, Sijia Liu, and Xiaomei Yu contributed equally to this work.) (Corresponding authors: Jianhong Wang; Jie Tian; Hui Hui.)*

Zechen Wei and Tao Zhu are with the CAS Key Laboratory of Molecular Imaging, Institute of Automation, School of Artificial Intelligence, Chinese Academy of Sciences, Beijing 100190, China, and also with the University of Chinese Academy of Sciences, Beijing 100190, China (e-mail: weizechen2019@ia.ac.cn; zhutao2020@ia.ac.cn).

Yanjun Liu, Haoran Zhang, and Bo Zhang are with the Key Laboratory of Big Data-Based Precision Medicine (Beihang University), Beijing 100190, China, and also with the School of Engineering Medicine and the School of Biological Science and Medical Engineering, Beihang University, Beijing 100190, China (e-mail: yanjunl@buaa.edu.cn; hrzhang@buaa.edu.cn; zhangbo1996@buaa.edu.cn).

Sijia Liu is with the School of Computer Science and Engineering, Southeast University, Nanjing 210000, China (e-mail: 230228519@seu.edu.cn).

Xiaomei Yu, Yali Zhang, Hongdi Huang, Yang Fan, Hongli Li, and Jianhong Wang are with the National Resource Center for Non-Human Primates, Kunming Primate Research Center, Kunming Institute of Zoology, Chinese Academy of Sciences, Kunming 650000, China, and also with the National Research Facility for Phenotypic and Genetic Analysis of Model Animals (Primate Facility), Kunming Institute of Zoology, Chinese Academy of Sciences, Kunming 650000, China (e-mail: yuxiaomei@mail.kiz.ac.cn; zhangyali@mail.kiz.ac.cn; huanghongdi@mail.kiz.ac.cn; fanyang@mail.kiz.ac.cn; lihongli@mail.kiz.ac.cn; wangjh@mail.kiz.ac.cn).

Jie Tian is with the Key Laboratory of Big Data-Based Precision Medicine (Beihang University), Ministry of Industry and Information Technology of the People's Republic of China, School of Engineering Medicine, Beihang University, Beijing 100190, China, also with the School of Biological Science and Medical Engineering, Beihang University, Beijing 100190, China, and also with the National Key Laboratory of Kidney Diseases, Beijing 100853, China (e-mail: tian@ieee.org).

Hui Hui is with the CAS Key Laboratory of Molecular Imaging, Institute of Automation, Chinese Academy of Sciences, Beijing 100190, China, also with Beijing Key Laboratory of Molecular Imaging, School of Artificial Intelligence, University of Chinese Academy of Sciences, Beijing 100190, China, and also with the National Key Laboratory of Kidney Diseases, Beijing 100853, China (e-mail: hui.hui@ia.ac.cn).

Digital Object Identifier 10.1109/TIM.2024.3418109

I. Introduction

MAGNETIC particle imaging (MPI) stands out as a novel imaging method capable of mapping the concentration distribution of superparamagnetic iron oxide nanoparticles (SPIOs) [1]. This noninvasive technique has advantages of real-time imaging, high sensitivity, and high spatial resolution, making it invaluable in applications, such as cell tracking, tumor detection, and perfusion imaging [2], [3], [4], [5], [6]. Quantification is a particular strength of MPI, given its high sensitivity as an imaging modality [7], [8]. Accurate reconstruction of SPIO distribution opens doors to diverse applications, including bleeding detection [9] and plaque identification [10].

In the development of MPI technique, different systems exploited the different advantages of MPI. Gleich et al. [11] utilized Lissajous trajectory to achieve 2-D real-time imaging, obtaining a frame rate of 25 frames/s. Then, the same team achieved 3-D real-time in vivo imaging [12], at a temporal resolution of 21.5 ms for a field of view (FOV) of $20.4 \times 12 \times 16.8$ mm^3. Besides, the high sensitivity of MPI method was proved by Graeser et al. [13], using a gradiometric receive coil, capable of detecting down to 5 ng$_{Fe}$. In addition, with pulsed excitation, submillimeter spatial resolution was achieved based on X-space [14] and system matrix [15] reconstruction method.

As mentioned above, the majority of equipment has been tailored to the mouse/rat scale [12], [16], [17], [18], [19], [20], exemplified by commercially available systems such as Magnetic Insight's (Alameda, CA, USA) [21]. Recently,

© 2024 The Authors. This work is licensed under a Creative Commons Attribution-NonCommercial-NoDerivatives 4.0 License.
For more information, see https://creativecommons.org/licenses/by-nc-nd/4.0/

efforts have been directed toward upscaling MPI systems. The Preclinical Bruker MPI system [21], applicable for mice- to rabbit-scale imaging, sports a 120-mm bore size and can cover an FOV of 56 × 56 × 56 mm^3. In addition, Le et al. [22] introduced a rabbit-scale system featuring a 90-mm bore size and a 56 × 56 × 56 mm^3 FOV at the maximum gradient of 4 T/m/μ_0. Achieving a temporal resolution of 1 frame/s for 2-D image and a spatial resolution of 7 mm, this system sets a notable standard. The challenge in expanding MPI systems lies in preserving their inherent advantages of high sensitivity, resolution, and real-time imaging, without adding complexity that might compromise system stability. To address this challenge for human-scaled MPI systems, various techniques have been explored. The research group at Phillips pioneered the development of the first human scanner. Then, a human-sized system is also designed for brain applications [23]. Tailored to fit an adult's head, this system achieves a bore size ranging from 19 to 25 cm, offering an FOV of 100 × 140 × 140 mm^3. The system can provide a detection limit of approximately 14.7 ng_{Fe}/mL and a spatial resolution of around 5 mm. In addition, superconductor is utilized to generate a gradient of 2.5 T/m/μ_0 for the system with a bore size of 200 mm, showcasing the potential for human application of MPI [24].

The primary motivation behind the designed structure in our study stems from the significant technical challenges encountered in developing NHP-sized MPI systems, particularly the quadratic increase in power consumption associated with electromagnetic coils. The human-brain-sized MPI scanner addressed this issue by employing an electromagnet structure to generate a dynamic selection field [23], significantly reducing system power consumption compared to pure electromagnetic coils. However, this structure exhibited limitations in terms of FOV size and temporal resolution for 3-D imaging. Furthermore, the presence of an iron core led to nonlinear interferences, leading to increased shielding costs.

In this study, we engineered the first NHP-MPI designed for applications involving primates [25]. Tailored to accommodate the size of primates' brain, our system features a substantial bore size of 190 mm, enabling a 3-D FOV of 120 × 120 × 120 mm^3. In the article, we conducted a comprehensive performance evaluation of the system [26], specifically in terms of sensitivity and spatial resolution. From the experimental results, the limit of detection of our system is approximately 19 μg_{Fe}. Also, we have proved the uniformity of sensitivity over the FOV. Notably, our NHP-MPI demonstrated good quantitative performance in imaging experiments, indicating its capability for high-sensitivity imaging that meets application requirements. Besides, our system achieved the spatial resolution of 8, 16, and 8 mm in the (x, y, z) direction, respectively.

The evaluation results of sensitivity and spatial resolution lay the foundation for subsequent applications on primate brain. To further validate the performance of our system, we conducted imaging experiments of a macaque' brain. The experiments were carried out at three-month intervals on a macaque, revealing that our system excels in effectively conducting 3-D imaging of the NHP.

TABLE I
PARAMETERS OF THE COILS IN OUR SYSTEM

Types	Turns	Total inductance	DC resistance
Drive coil & compensation drive coil	78+34	1.45 mH	0.28 Ω
Focus coils (y)	52×2	1.67 mH	0.30 Ω
Focus coils (z)	1132×2	\	3.65 Ω
Receive coil	16	42.66 μH	0.17 Ω
Compensation receive coil	25	223.1 μH	0.31 Ω

II. METHOD

Building on previous experiences, we designed a system structure that combines permanent magnets with electromagnetic coils. The permanent magnets efficiently generate the selection field, thereby reducing the need for excessive current and minimizing power consumption. Meanwhile, the electromagnetic coil component enables flexible driving of the FFP for rapid 3-D scanning.

By integrating these two components, our design offers a balance between power efficiency and imaging capabilities. The permanent magnets provide a stable selection field, while the electromagnetic coils provide the necessary flexibility for precise and rapid scanning. This combination allows us to overcome the limitations of previous approaches and develop an NHP-MPI that is both power-efficient and capable of performing 3-D imaging with a large FOV.

A. Coil Configuration

The coil configuration of the proposed 3-D NHP-MPI system is illustrated in Fig. 1. From Fig. 1, the system comprises six main components: permanent magnets, z-direction focus coils, y-direction focus coils, drive coil, receive coil, and compensation coils. The parameters of the coils are listed in Table I.

The basic idea of the scanner design follows the classic field-free point (FFP) MPI scanner scheme [1]. From Fig. 1(a), the system incorporates two circular NdFeB permanent magnets with opposite polarities symmetrically fixed to the upper and lower sides of the FOV. Each circular permanent magnet has an outer diameter of 200 mm, an inner diameter of 96 mm, and a height of 20 mm. This arrangement generates a linear gradient magnetic field and an FFP, as depicted in Fig. 1(b). The linear gradient magnetic field and FFP are essential for the functioning of the system. In order to make the FOV cover the whole brain of NHPs, we have adopted the focused field approach [12]. To enable FFP movement and scanning along the z-axis, a pair of Helmholtz coils is employed to generate a focus field in the z-direction. From Fig. 1(c), the y-direction focus coils adopt a saddle-shaped structure, enhancing compactness and ensuring the production of a uniform y-direction magnetic field that facilitates FFP

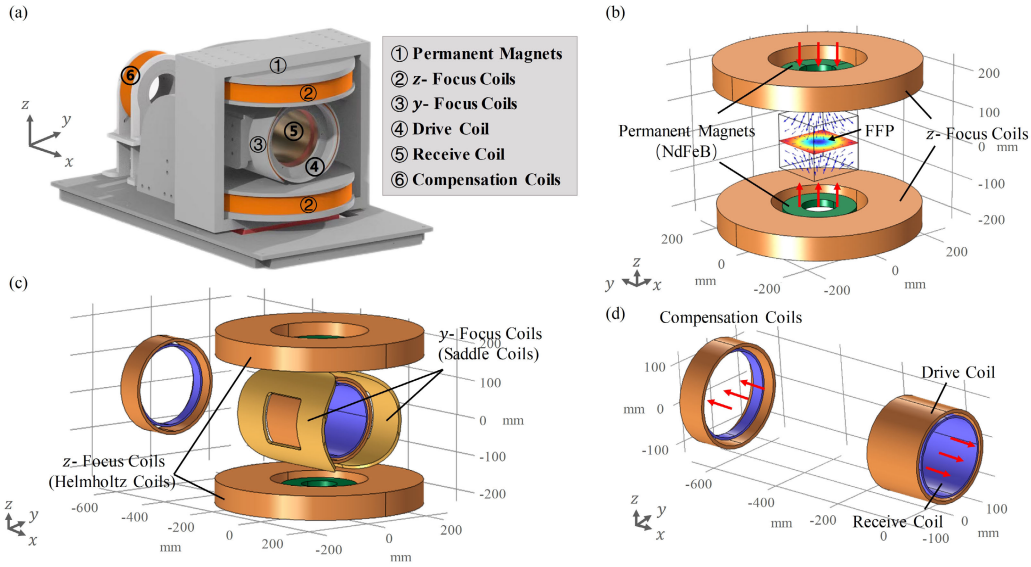

Fig. 1. Coil topologies of the proposed MPI system. (a) Overall structure. (b) NdFeb permanent magnets for field-free point (FFP) generation. (c) z-focus coils and y-focus coils. (d) Drive coil, receive coil, and compensation coils.

movement and scanning along the y-axis. Fig. 1(d) reveals the drive and receive coils, which are presented as a pair of coaxial solenoids along the x-direction. The drive coil is responsible for generating an alternating magnetic field to excite the dynamic magnetization response of particles. Meanwhile, the receive coil generates a voltage signal through electromagnetic induction. To mitigate direct feedthrough from the drive field, additional compensation coils are implemented, which are similar to the gradiometric coils [13]. These coils, situated at a greater distance from the drive and receive coils, include both transmit and receive coils. They work together to generate a compensation signal with an amplitude equal to that of the direct feedthrough signal but with a phase difference of 180°. This compensation signal is utilized to cancel out the direct feedthrough signal before the received signal enters the preamplifier. The positioning of the compensation coils at a farther distance helps to avoid magnetic field coupling. In summary, the described coil configuration is a crucial element of the NHP-MPI system, enabling precise control of magnetic fields for imaging purposes while addressing challenges, such as direct feedthrough and magnetic field coupling.

B. Digital Scanning Method

In traditional methods, the focus field is often described as a function of the FFP position, resulting in a bias field with opposite polarity to the desired FFP position. Point-by-point scanning is achieved by adjusting the amplitude of the bias field. However, due to the time-consuming nature of magnetic field switching, 3-D point-by-point scanning can be inefficient. To address this, we adopt a line-by-line scanning sequence to enhance the scanning speed. The working mechanism of the scanning sequences is shown in Fig. 2.

By passing a triangular wave current with a specific frequency through the y-direction coils, a linearly varying

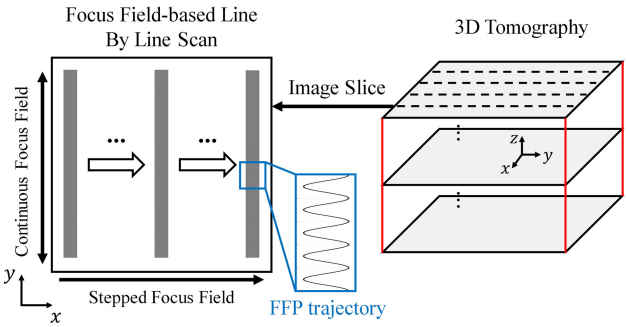

Fig. 2. Illustration of the working mechanism of the proposed focus field-based line-by-line scanning of our system.

alternating magnetic field is generated. This design has similarities to the scan sequences used previously in the Berkeley scanner [18] and traveling-wave MPI [27], which causes the FFP to swiftly move along the y-direction. While theoretically, the x- and z-directions could also use alternating magnetic fields to further enhance the scanning speed, it would necessitate additional power, and the scanning trajectory density would be compromised. The focus field utilized in this study is represented as follows:

$$\begin{aligned}&\boldsymbol{H}^{\mathrm{F}}\left(t, x^{\mathrm{FFP}}, z^{\mathrm{FFP}}\right)\\&= -G_x x^{\mathrm{FFP}}\boldsymbol{e}_x - G_y|y_{\mathrm{FOV}}|\mathrm{tri}\left(2\pi f_y t\right)\boldsymbol{e}_y - G_z z^{\mathrm{FFP}}\boldsymbol{e}_z \end{aligned} \quad (1)$$

where x^{FFP} and z^{FFP} represent the x- and z-coordinates corresponding to the current position of FFP, respectively; and G_x, G_y, and G_z represent the field gradient in (x, y, z) directions, respectively. $\mathrm{tri}(2\pi f_y t)$ is created as a triangular wave function with frequency f_y and $-1 \le \mathrm{tri}(2\pi f_y t) \le 1$, and $|y_{\mathrm{FOV}}|$ is the absolute value of the edge coordinates in the y-direction of FOV. The one-way scan time is $1/(2f_y)$ for a single line. For example, if f_y is set to 10 Hz, the shortest time required to scan a line is 50 ms. Then, to achieve 2-D

expansion and 3-D slice selection, stepwise focus fields are applied along the z- and x-directions based on the desired scanning step size. A more power-efficient alternative involves using moving objects instead of biasing magnetic fields. In this study, the x-direction expansion is accomplished by moving the imaging bed, while the z-direction layer selection is achieved using electromagnetic coils to generate a biasing magnetic field. Therefore, for the sampling time $t \in [0, T^S]$ of the ith scan line in the jth slice, the total magnetic field in the FOV can be described as follows:

$$\boldsymbol{H}_{ij}^{\mathrm{FOV}}(\boldsymbol{r},t) = H^D(t)\boldsymbol{e}_x + H_y^F(t)\boldsymbol{e}_y + G_x\left(x - x_i^{\mathrm{FFP}}\right)\boldsymbol{e}_x + G_z\left(z - z_j^{\mathrm{FFP}}\right)\boldsymbol{e}_z \quad (2)$$

where $\boldsymbol{r} = [x, y, z]^T$, T^S is defined as the sampling time of a single scan line, and alternating focus field $H_y^F(t) = -G_y|y_{\mathrm{FOV}}|\mathrm{tri}(2\pi f_y t)$ in the y-direction.

C. Imaging Method

Under excitation by an alternating magnetic field, MNPs generate a dynamic magnetic response detected by a receive coil to produce an induced voltage signal. The voltage signal of the ith scan line within the jth slice can be expressed as

$$u_{ij}(t) = -\mu_0 p^R \int_{\mathrm{FOV}} c(\boldsymbol{r}) \frac{\partial M\left[\boldsymbol{H}_{ij}^{\mathrm{FOV}}(\boldsymbol{r},t)\right]}{\partial t} d\boldsymbol{r} \quad (3)$$

where μ_0 is the vacuum permeability, p^{R} is the receive coil sensitivity, $c(\boldsymbol{r})$ is the particle concentration distribution, and M is the magnetization. Due to the nonlinear response characteristics of the MNPs, the voltage signal contains harmonic components in addition to the fundamental frequency component. Typically, these harmonic signals have a higher spatial frequency, contributing to achieving high-resolution imaging. In traditional methods, the voltage signal can be directly Fourier-transformed to obtain the harmonic spectrum in the frequency domain. However, this harmonic spectrum generally represents the aggregation of harmonic signals from all MNPs in the entire FOV and cannot be mapped to specific spatial locations. To address this limitation, we adopt the short-time Fourier transform (STFT) technique to process the acquisition signals of each scan line, obtaining the harmonic signals within each time window T^{W}. The overall process is described as follows:

$$\widehat{u}_{ij}\left(k, \tilde{t}_n\right) = \int_{\tilde{t}_n - T^W/2}^{\tilde{t}_n + T^W/2} u_{ij}(t) e^{-\mathrm{i}2\pi k f^{\mathrm{D}} t} dt \ , t \in \left[0, T^S\right] \quad (4)$$

where $\widehat{u}$ denotes the harmonic signal and k is the harmonic order.

The time window of STFT divides the scan line into N segments, $\tilde{t}_n$ represents the center time of the nth segment, and $T^S = NT^W$. A rectangular window function is utilized, and symbol i denotes the imaginary unit, distinct from the index i. Since the focus field in the y-direction changes linearly, the displacement Δy of the FFP in the y-direction within each time window is the same. By setting T^W small enough, Δy can be restricted to a pixel size, and the central coordinate of the nth displacement is defined as y_n^{FFP}.

Because of the line-by-line scanning sequence adopted in this study, both 2-D scanning and 3-D scanning are employed to process the line-scan signal. Based on the preset FFP motion trajectory, the harmonic signal is mapped to the corresponding spatial position. This process can be understood as the x-space approach [28] that combines single harmonic signal acquisition and mapping

$$\widehat{u}_k\left(x_i^{\mathrm{FFP}}, y_n^{\mathrm{FFP}}, z_j^{\mathrm{FFP}}\right) = \widehat{u}_{ij}\left(k, \tilde{t}_n\right) \quad (5)$$

where $\widehat{u}_k$ represents the kth harmonic signal in the image domain, also known as the kth harmonic map.

The weighted sum of harmonics (WSH) is used for direct imaging of the spatial distribution of MNPs. WSH offers advantages, such as no complex calibration or computation requirements, providing balanced spatial resolution and adjustable signal-to-noise ratio (SNR). The details of the method can be found in previous work [29], and the imaging formula is expressed as follows:

$$I\left(\boldsymbol{r}^{\mathrm{FFP}}\right) = \sum\nolimits_{k=K_L}^{K_H} w_k \hat{u}_k\left(\boldsymbol{r}^{\mathrm{FFP}}\right), \ k \in \mathbb{N}, \ K_H \geq K_L \geq 1 \quad (6)$$

where $\boldsymbol{r}^{\mathrm{FFP}} = (x_i^{\mathrm{FFP}}, y_n^{\mathrm{FFP}}, z_j^{\mathrm{FFP}})$ and w_k denotes the weight of the kth harmonic. K_L and K_H indicate the lowest and highest harmonic orders used, respectively, which are generally determined by the signal bandwidth. For example, the 3rd and 5th harmonics are used in this study, i.e., $K_L = 3$ and $K_H = 5$. The weight function based on the normalization of odd-harmonic energy proposed in previous studies [29] balances spatial resolution and SNR but lacks particle concentration quantization. An improvement is introduced by multiplying the 2-norm of a lower order harmonic map

$$w_k = (-1)^{k-1} \frac{\|\widehat{u}_{K_L}\left(\boldsymbol{r}^{\mathrm{FFP}}\right)\|_2}{\|\widehat{u}_{2k-1}\left(\boldsymbol{r}^{\mathrm{FFP}}\right)\|_2} \ , k \in N \quad (7)$$

where $\|\cdot\|_2$ represents the Euclidean norm. The symbol $(-1)^{k-1}$ is attributed to the alternating negative and positive of the odd-harmonic signal. Therefore, the mathematical expression from signal to image is

$$I\left(\boldsymbol{r}^{\mathrm{FFP}}\right) = \hat{u}_3\left(\boldsymbol{r}^{\mathrm{FFP}}\right) - \frac{\|\hat{u}_3\left(\boldsymbol{r}^{\mathrm{FFP}}\right)\|_2}{\|\hat{u}_5\left(\boldsymbol{r}^{\mathrm{FFP}}\right)\|_2} \hat{u}_5\left(\boldsymbol{r}^{\mathrm{FFP}}\right). \quad (8)$$

III. System Design

The system coils are meticulously designed as a sealed-off cylindrical structure, with a selected bore size of 190 mm tailored for NHP-scale applications. The 3-D FOV is defined as 120 × 120 × 120 mm^3. The selection field gradient is set to (0.1, 0.1, −0.2) T/m/μ_0 along the x-, y-, and z-axes, respectively. Consequently, the system is anticipated to achieve a spatial resolution of approximately 10 mm, aligning with the requirements for primate-brain imaging applications [23]. The drive field is configured at 5 kHz with an amplitude of 6 mT/μ_0. Both the frequency and amplitude of the drive field are meticulously chosen below the magneto-stimulation threshold for peripheral nerve stimulation (PNS) in our NHP-MPI. In addition, the frequency of the focus field along the y-direction is set at 10 Hz with an amplitude of 6 mT, allowing the FFP to move within a range of ±60 mm. To mitigate direct

feedthrough signals from the drive field, we have incorporated external compensation coils. These coils, along with transmit and receive coils, generate a compensation signal with an amplitude equal to that of the direct feedthrough signal but with a phase difference of 180°. The external transmit/receive coils are interconnected in series with the drive/receive coils.

Parameters of the coils and the resulting magnetic fields are simulated using COMSOL Multiphysics software (COMSOL, Stockholm, Sweden), while the physical structure is meticulously engineered using CAD software (Solidworks, MA, USA). The MPI system encompasses a preamplifier, a signal transmission and data acquisition system with a digital-to-analog converter (DAC) and an analog-to-digital converter (ADC), power amplifiers, and a mechanical displacement device (refer to Fig. 3). The maximum movement distance of the mechanical displacement device [see Fig. 3(c)] in the x-direction is 500 mm, which enables the bed to move throughout the entire range of the receive coil. Also, the minimum step width of the device is 0.1 mm, which is sufficient for the imaging experiments.

All transmit coils are powered by the AE Techron 7548 power amplifiers (3.3 kW; AE Techron). The receive coil and external compensation receive coil are wound in opposite directions and connected in series to minimize direct feedthrough signals from the drive field. Following this, they are preamplified (SR560, SRS, Sunnyvale, CA, USA) before digitization. The drive coil and compensation drive coil, connected in series, are linked to the power amplifier with a resonant frequency of 5 kHz.

The selection fields in three axial directions were measured using a Gauss meter (FW Bell, Portland, USA). The measured values were compared with simulation results (see Fig. 4). In addition, based on the data in Fig. 4(a), field gradients were calculated, as illustrated in Fig. 4(b).

From Fig. 4(a), the measured selected field is basically consistent with the simulation values. Besides, from Fig. 4(b), the gradient is not strictly linear and has deviations. The nonuniformity of gradients may cause distortion in the reconstructed image. In summary, we believed that the system achieved a gradient of approximately 0.1 T/m/μ_0 in the x- and y-axes and approximately -0.2 T/m/μ_0 in the z-axis.

For signal transmission and data acquisition, NI PXIe-6374 from National Instruments (Austin, TX, USA) was employed, operating at a sampling rate of 1.00 MS/s. System control, data collection, processing, and image reconstruction were carried out using LabVIEW (National Instruments) and MATLAB software (MathWorks, Inc., Natick, MA, USA).

IV. Experiment Setup

A. Phantom Experiments

The experimental setup is detailed in this section, utilizing Synomag particles (Micromod GmbH, Germany) with a dextran surface and an equivalent distribution of particle diameters at 70 nm.

1) Sensitivity Analysis: A dilution series of Synomag particles was created with total volumes of 500 μL and an iron mass ranging from [4.88, 312.5] μg, corresponding to Fe concentrations of [0.0098, 0.625] $\mu g/\mu$L. As a control, the signal of 500-μL water was also collected. The dilution series was created by continuously diluting twice from the original solution. For the sensitivity experiment, the standard mode of the system was employed, where $G(x, y) = (0.1, 0.1)$ T/m/μ_0, f_x =5 kHz, f_y =10 Hz, f_{sample} =1 MS/s, and the acquisition time for each image is 1 s. Based on the PNS limits of human [30] and the related analysis of the PNS limits [28], [31], also with the consideration of MRI experiments on primates [32], we set the amplitudes of the drive field (x-axis) and the focus field (y-axis) to 6 mT. Thus, an FOV of 120 × 120 mm^2 was created. For reconstruction, we averaged the signals (1 s) and interpolated the reconstructed image to 120 × 120, with each pixel size of 1 mm.

2) Spatial Resolution Analysis: The spatial resolution of NHP-MPI was designed to be better than 10 mm to provide sufficient image details for brain applications. Two elongated phantoms containing Synomag at a concentration of c_{Fe} = 10 mg/mL were designed to evaluate spatial resolution. The distance between the two phantoms varied from 6 to 24 mm (edge to edge), with the chamber size being 5 × 5 × 15 mm^3. For the x- and y-axes, the phantoms were placed at the center of the xy plane, while for the z-axis, the phantoms were in the yz plane. The 2-D MPI imaging sequences were collected.

In addition, we conducted an assessment of the point spread function (PSF) of the system. Utilizing the dot phantom with a size of 5 × 5 × 5 mm^3, we employed a phantom considerably smaller than the expected resolution of our system, allowing it to be treated as a point source. For imaging, the phantom was positioned at the center of the FOV in the xy plane and a 2-D image was recorded.

For the spatial resolution experiment, a high-resolution mode was employed. By introducing two opposing direct current into the z-direction focus coils, the gradient strength of the selection field was increased to $(0.3, 0.3, -0.6)$ T/m/μ_0 in (x, y, z) direction. With the same drive field and y-direction focus field parameters as in the standard mode, high-resolution imaging was achieved over a local FOV of 40 × 40 mm^2. The scanning step size was 2 mm, and the time taken to scan each line was 1 s. Therefore, for the 2-D high-resolution mode, the scanning time was approximately 20–40 s. Finally, each reconstructed image was interpolated to 40 × 40 pixels, with each pixel representing a size of 1 mm.

B. Animal Experiments

The imaging experiments were carried out on a male adult macaque (*Macaca mulatta*) weighing 8.50 kg and aged 12 years, sourced from breeding colonies at the Kunming Institute of Zoology for the animal experiment. The macaque was individually housed under standard conditions, maintaining a temperature of 21 ± 5 °C and a humidity at 60%, with a 12 h light/dark cycle (light on from 07:00 to 19:00 h). The macaque had unrestricted access to tap water, punctually received standard chow foods twice a day and was provided with fresh fruits or vegetables once a day. Experiments were conducted between 9:00 and 17:00 h, following the guidelines

Fig. 3. NHP-MPI system. (a) Front view. (b) Side view. (c) Mechanical displacement device. (d) Preamplifier. (e) and (f) Signal transmission and data acquisition system with a digital-to-analog converter (DAC) and an analog-to-digital converter (ADC). (g) Power amplifiers.

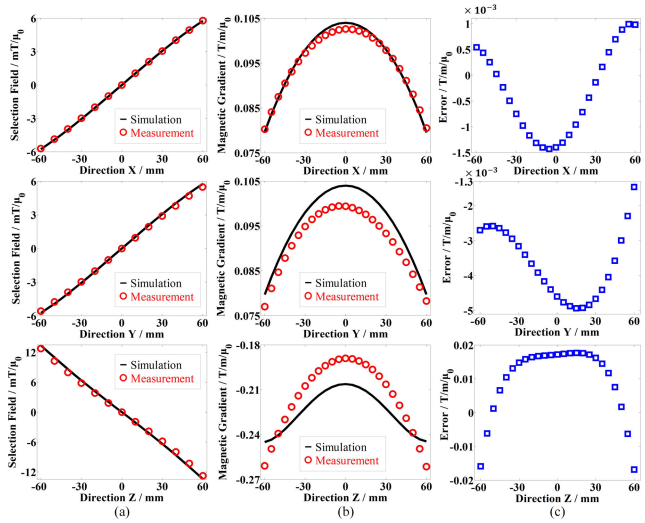

Fig. 4. Simulated and measured selection field and gradients. (a) Selection field in three axial directions. The measurement is conducted using a Gauss meter (FW Bell 5180, Portland, USA). (b) Selection field gradient calculated from the data in (a). (c) Error between simulation and measured gradient strength in (b). The system achieves a gradient strength of 0.1 T/m/μ_0 in the x- and y-axes and -0.2 T/m/μ_0 in the z-axis.

outlined in the Application Format for Ethical Approval for Research Involving Animals (IACUC-PE-2023-09-001). All necessary measures were taken to minimize the number of animals used and reduce animal suffering.

MPI data were collected at the National Research Facility for Phenotypic and Genetic Analysis of Model Animals (Primate Facility), Kunming Institute of Zoology, in the macaque, on two occasions with a three-month interval. The macaque was anesthetized using hydrochloric acidulated ketamine (Jiangsu Zhongmubeikang Pharmaceutical Company Ltd., 10 mg/kg, i.m.) and maintained with propofol (Guangdong Jiabo Pharmaceutical Company Ltd., 25 mg/kg/h i.v.) during MPI scanning. Atropine (Henan Runhong Pharmaceutical Company Ltd., 0.05 mg/kg, i.m.) was administered 10 min before anesthesia to reduce salivation. The macaque underwent a 12-h fasting period before the experiment.

For animal experiment, the standard mode was employed to record 3-D imaging sequences, where $G(x, y, z) = (0.1, 0.1, -0.2)$ T/m/μ_0, $f_x = 5$ kHz, $f_y = 10$ Hz, and $f_{\text{sample}} = 1$ MS/s. A 3-D FOV of $120 \times 120 \times 120$ mm^3 was scanned. The step width was 6 mm in the z-axis. Thus, 21 lines along the z-axis were collected, with 1-s acquisition time of each line. Finally, each 3-D image was interpolated to $120 \times 120 \times 120$, with each pixel size of 1 mm.

V. Results

A. Sensitivity Results

The dilution series and the corresponding 2-D images are illustrated in Fig. 5. As depicted in Fig. 5, the sample ranging from 312.5 μg_{Fe} down to 19.53 μg_{Fe} is detectable. Consequently, the sensitivity limitation of our system is approximately 19.53 μg_{Fe}.

Besides, to assess the quantitative performance of our system, we calculated the average value of the reconstructed image (see Fig. 6). Results in Fig. 6 reveal that our system exhibits satisfactory quantitative capabilities. The dilution series is generated by halving the previous concentration, and this relationship is reflected in the values of the reconstructed image.

To evaluate the uniformity of sensitivity over the FOV, we chose the maximum iron mass (312.5 μg_{Fe}) and the minimum iron mass (19.53 μg_{Fe}) that can be detected in Fig. 5 for further experiments. As shown in Fig. 7, the sensitivity phantoms were placed at three positions on the diagonal of the FOV. From the results, although the appeared artifacts led to degradation in the image quality, the phantom with iron mass as low as 19.53 μg_{Fe} could still be detected, and the

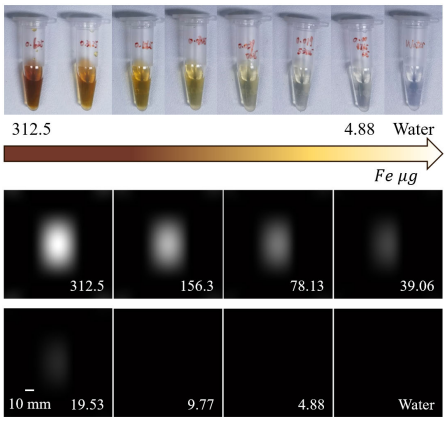

Fig. 5. Sensitivity results. (Top) Synomag dilution series with iron mass ranging from 4.88 to 312.5 μg_{Fe}, using the same water phantom for reference. (Bottom) Corresponding reconstructed image of Synomag dilution series. All images were globally normalized before visualization.

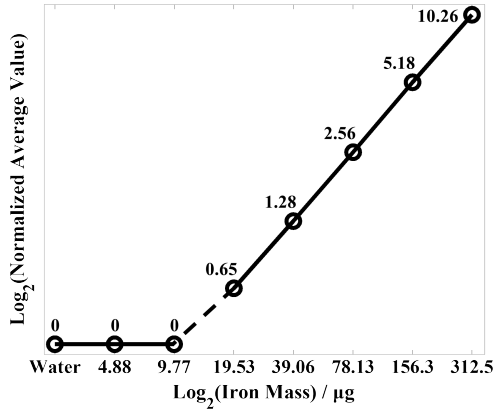

Fig. 6. Average value of the reconstructed image. All images were first globally normalized before averaging. The axes were converted to logarithmic coordinates with a base of 2. The numbers of x-coordinates and above the curve represented the value before calculation.

movement from the lower right to the upper left in the FOV could be observed. Meanwhile, after global normalization, the values of reconstructed images from different positions were all of the same order of magnitude, which proved the detection limit (19.53 μg_{Fe}) of our system and uniformity of sensitivity over the FOV in our system.

B. Spatial Resolution Results

Spatial resolution experiment results are presented in Fig. 8. It is evident from Fig. 8 that our NHP-MPI can resolve two objects with a minimum spacing of 8 mm in the x-direction [see Fig. 8(b)], 16 mm in the y-direction [see Fig. 8(c)], and 8 mm in the z-direction [see Fig. 8(d)]. In addition, the examination of line profiles in the images demonstrates the system's ability to clearly distinguish between two phantoms with different distances. For the x-direction, two samples at 8-mm distance can still be differentiated from the two peaks, while 6-mm phantoms are completely indistinguishable. For the other two directions, the corresponding minimum resolution can also be obtained from the line profiles.

Furthermore, we conducted tests on the system's PSF, as shown in Fig. 9. The measured PSF is approximately

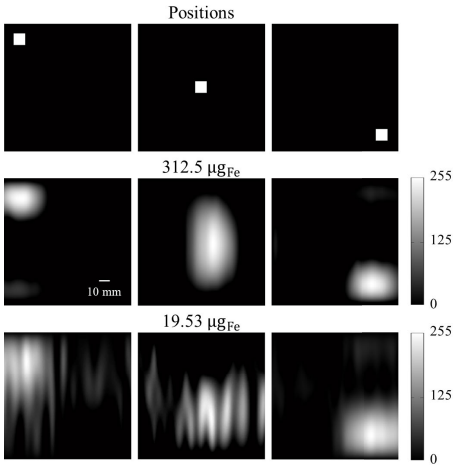

Fig. 7. Results of sensitivity uniformity over the FOV. The phantoms were placed at the three positions of the diagonal in the FOV (top three images). We imaged the sensitivity phantom with an iron mass of 312.5 μg_{Fe} (middle three images) and 19.53 μg_{Fe} (bottom three images) in the three positions. The imaging results for each concentration were first globally normalized before visualization.

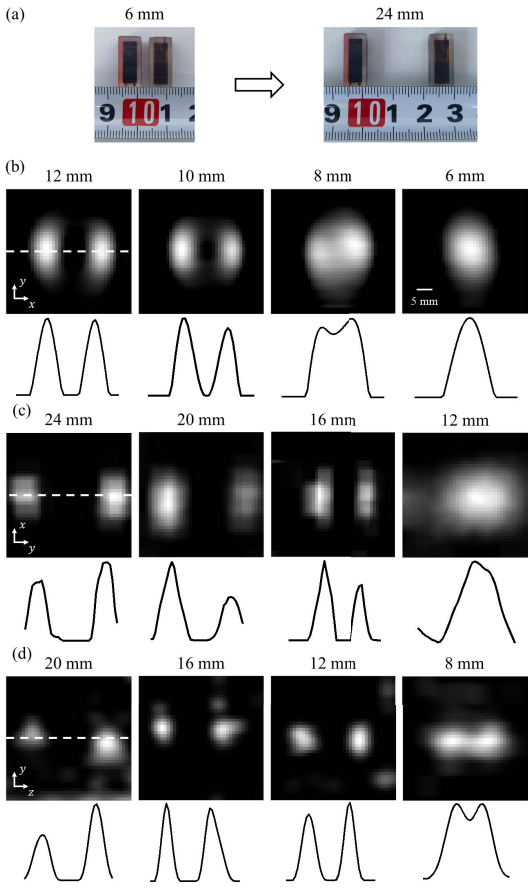

Fig. 8. Spatial resolution of the system. (a) Phantoms at different distances ranging from 6 to 24 mm. (b)–(d) Reconstructed images and line profiles of the resolution phantoms in the x-, y-, and z-directions, respectively.

9 mm, which is consistent with the spatial resolution in the x-direction.

C. Imaging Results of Animal Experiments

In the imaging experiment, a macaque was intravenously with 4 mL of 10-mg_{Fe}/mL Synomag particles (over 20 s)

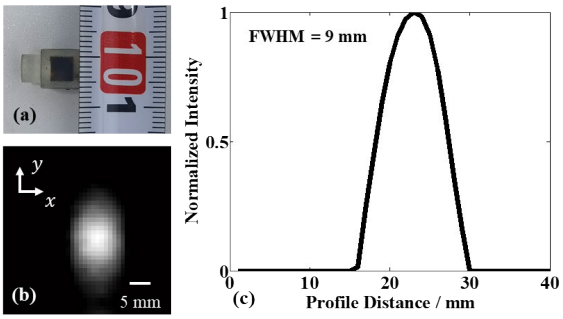

Fig. 9. (a) Dot phantom. (b) Measured PSF. (c) Line profiles of the 1-D collinear component.

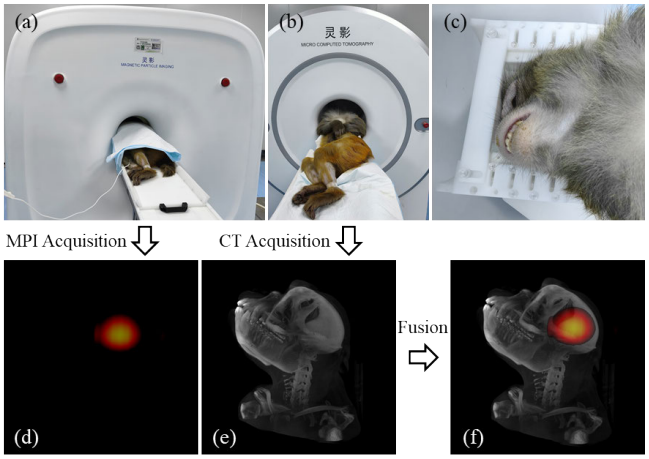

Fig. 10. Illustration of (a) MPI and (b) CT acquisition, with (c) showcasing the brace affixed to the macaque's head. (d) and (e) MPI image and CT image, respectively. (f) Representative 3-D fusion image.

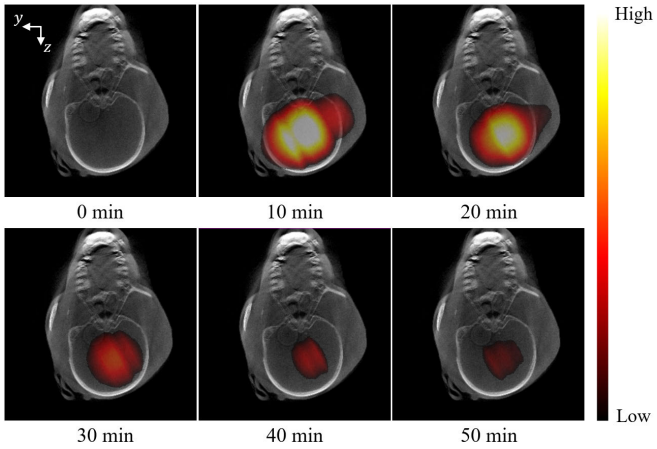

Fig. 11. Visualization of the fusion image at different time points, exemplified by the 188th layer of the fused 3-D image.

under anesthesia. The initial injection time was set to 0 min, and a 3-D MPI image was captured every 10 min to observe particle distribution in the macaque's brain. The total duration of the experiment was 50 min, and the experiments were repeated twice with a three-month interval. Based on the previous works [25], [33], in the first experiment, particles were injected twice (2 mL at 0 min and 2 mL at 30 min), while in the second experiment, particles were injected once (4 mL) at 0 min. Thus, the total dose injected was about $4 \times 10/8.5 = 4.7$ mg_{Fe}/kg, which was two times less than the typical 10-mg_{Fe}/kg dose of SPIOs used in fMRI studies [32]. All other procedures remained consistent across the two experiments.

In the experiments conducted, we integrated the acquired 3-D MPI images with pre-collected computed tomography (CT) images to observe the distribution of magnetic particles within the macaque's brain. The CT parameters included a voltage of 90 kV, a current of 500 μA, an exposure time of 200 ms, a source detection distance of 590 mm, and a ray source to center of rotation distance of 313 mm. A total of 720 angles were collected during scanning, with four images captured from each angle for averaging. The resulting CT image had dimensions of 3072×3072 pixels and a pixel size of 0.139 mm.

During the experiments, the macaque's head was securely fixed using a brace [see Fig. 10(c)] to maintain a stable position with the bed. Following the animal experiments, the labeled brace was scanned to establish the conversion relationship between the MPI image and CT image for registration purposes. Before registration, a global normalization process was applied to all MPI images. The MPI images were then interpolated using the ImageJ package FIJI (fiji.sc/Fiji, NIH, Bethesda, MD, USA). Subsequently, the registration process was carried out. A representative 3-D fusion image was generated, as shown in Fig. 10(f).

The study proceeded to analyze the variation of magnetic particles in the macaque's brain over time. Specifically, focusing on the results from the second set of experiments, a representative slice of the yz plane was selected for analysis (see Fig. 11). Initially, no signal was detected at the beginning of the injection. As the injection progressed (lasting approximately 20 s), magnetic particles circulated through the macaque's body via the bloodstream, reaching the cerebral vessels. Consequently, a distinct signal was detected at 10 min. However, as the particles continued circulating in the bloodstream, they gradually achieved an even distribution throughout the vessels and underwent metabolism by the liver. This led to a gradual decrease in the concentration of particles within the vessels over time, as observed in Fig. 11. From the images captured between 20 and 50 min, the amount and intensity of the particles exhibited a gradual decrease, aligning with the dilution of concentration, and eventually reached a steady state. This observation serves to illustrate the dynamic changes in particle distribution within the cerebral vessels of the macaque.

Furthermore, we conducted a quantification of the values associated with each 3-D MPI volume in the two experiments. All 3-D volumes underwent global normalization, and the average values for each volume are illustrated in Fig. 12. The depicted trend in Fig. 12 reveals a gradual decrease in the concentration of particles, ultimately stabilizing at a steady state. This emphasizes the quantitative capability of our NHP-MPI system. Notably, both experiments yielded similar results under identical experimental conditions, highlighting the reliability and stability of our system.

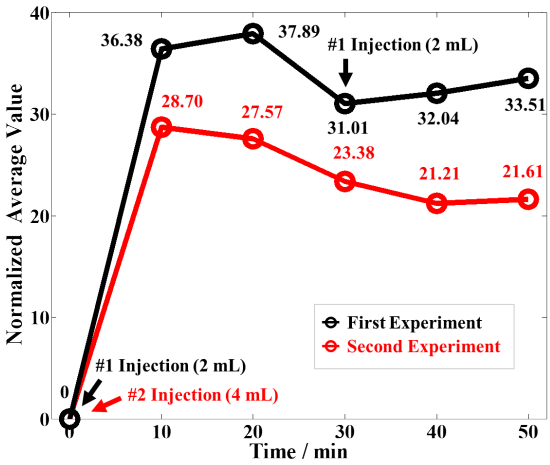

Fig. 12. Analysis of the average values of the 3-D MPI volume at various time points in two experiments. Prior to averaging, all 3-D MPI volumes underwent global normalization, ensuring uniformity in the analysis process.

VI. Discussion

In this work, we engineered an MPI system tailored for nonhuman primates, featuring a bore size of 190 mm and an FOV measuring 120 × 120 × 120 mm^3. The system excels in high-sensitivity real-time imaging, with a detection limitation of 19.53 μg_{Fe}. Moreover, the system exhibits the capability to resolve objects down to 8 mm. Our system also demonstrates satisfactory quantitative performance. In the imaging experiments involving the macaque brain, the 3-D volumes acquired by our system effectively depict the evolving distribution of particles within the brain over time, offering information for the fusion image with the CT image.

While our system serves as an advanced reference for systems with large bore sizes, its design can be enhanced to better suit clinical applications and accommodate a larger bore size. In our experiments, the system achieves a resolution of 8–10 mm, fulfilling the requirements for stroke detection applications, such as cerebral hemorrhage. However, applications, such as cell tracking and tumor detection, demand higher resolution. We employ a relatively small gradient field [(0.1, 0.1, −0.2) T/m/μ_0 along the (x, y, z) axis], which, to some extent, compromises spatial resolution. Cost considerations aside, one approach is to increase the volume of permanent magnets or employ electromagnets to generate higher gradients through high currents. However, due to volume and power limitations, directly elevating the gradient to a high level is unfeasible. Superconducting materials offer an alternative option [24]. In addition, the arrangement and combination methods of permanent magnets in a field-free-line (FFL) system can be considered [34], [35]. Furthermore, reference can be made to advanced models [36], [37], reconstruction algorithms [29], and deep-learning-based image postprocessing methods [38], [39], [40] to further enhance resolution.

Our system can achieve fast reconstruction. However, when using a shorter signal for reconstruction, the influence of background noise will also increase, further leading to degradation in image quality. The temporal resolution of our system is constrained by the frequency of the focus field. Increasing the frequency enables more information to be utilized for reconstruction within the same time, thereby reducing interference from background noise and improving spatial resolution. To further enhance temporal resolution while obtaining high-quality reconstruction, the following methods can be considered.

1) Increase the frequencies of the focus field. Employing a high-frequency digital focus field would be beneficial for reconstructing images from shorter time. However, when increasing the frequency, it is necessary to comprehensively consider its impact on the density of trajectory, which might lead to the degradation of spatial resolution.
2) Improve the sampling rate of our system, which currently operates at 1 MS/s. This approach allows for the full extraction of information from the signals, reducing quantization errors, and suppressing high-frequency noise, which might be beneficial for upgrading system and designing innovative imaging method, especially for some deep learning-based reconstruction methods [41], [42].
3) Implement advanced reconstruction algorithms and postprocessing methods [41], [42] to effectively suppress background noise, thereby improving image quality at high temporal resolutions.

In practical applications, achieving simultaneous improvements in sensitivity, spatial, temporal resolution, and the FOV of the system poses challenges. As mentioned earlier, enhancing temporal resolution may lead to a decline in image quality. Therefore, the performance of the system must be precisely designed based on specific applications. One viable solution involves employing different modes for different applications, such as a high-sensitivity mode for qualitative tasks and a high-resolution mode for quantitative tasks. For our NHP-MPI, where high sensitivity is crucial for macaque applications, future work can explore studying the sensitivity of different particles and designing new tracer materials for various disease models to enhance sensitivity in applications.

Heat dissipation is a common challenge in MPI scanners. Both the energized coils and the inductance of the excitation end in the system generate heat after prolonged operation. In the design of our NHP-MPI system, permanent magnets are utilized to replace electromagnetic coils, thus reducing the heat generated by electromagnetic coils. In addition, the current amplitudes of other electromagnetic coils are strictly controlled to below 30 A. These configurations enable the current version of the scanner to operate stably for extended periods. Nevertheless, as technology advances and scanner performance requirements increase, additional heat dissipation measures may become necessary. In the future, we plan to explore various heat dissipation solutions, such as integrating cooling fans, heat sinks, or even liquid cooling systems.

To demonstrate the advantages of our NHP-MPI system, it was compared with the human-sized system [23] and the rabbit-scaled system [22] (see Table II). Our NHP-MPI has a higher maximum gradient than the human-sized MPI (0.6 T/m/μ_0 compared to 0.2 T/m/μ_0), and the AM-MPI achieves the highest maximum gradient (4 T/m/μ_0). However, our NHP-MPI and human-sized MPI have a bore size twice larger than AM-MPI and offer a much bigger FOV under low

TABLE II
COMPARISON OF DIFFERENT MPI SYSTEMS

Category	Human-sized MPI [23]	AM-MPI [22]	NHP-MPI
Bore size (mm)	190-250	90	190
Field free region	FFP	FFP	FFP
Maximum gradient in (x, y, z) axes (T/m/μ_0)	(0.1, 0.2, 0.1)	(4, -2, -2)	(0.3, 0.3, -0.6)
Maximum FOV (mm^3)	100×140×140	89.6×89.6×89.6	120×120×120
Spatial resolution in (x, y, z) axes	(5, 6, 26)	(7, 15, 8)	(8, 16, 8)
Total power required	~1-2 kW	65 kW	~1 kW

gradient. Besides, NHP-MPI also achieves similar spatial resolution under lower gradient. Also, the human-sized MPI even achieves a better spatial resolution in the x- and y-directions than AM-MPI. In addition, the permanent magnets applied in our system efficiently reduce the need for excessive current and minimize power consumption. For a standard 3-D imaging sequence, the average power of the drive coils, y-focus coils, and z-focus coils is 120, 85.5, and 178.85 W, respectively, leading to a total power required of 384.35 W. Compared to the AM-MPI, our NHP-MPI reduces the demand for power consumption and achieves the imaging of NHP animals.

In our research, we conducted preliminary experiments applying our NHP-MPI to imaging the macaque's brain, yielding promising quantitative results. Subsequent endeavors will involve further exploration of the application in different disease models and the half-life time of different particles in animal experiments, where the dose of SPIOs will be further determined based on the specific application and experiment. Furthermore, the quantitative capabilities of our system hold potential for serving as functional MPI (fMPI), which is a new multimodal functional imaging modality [33], [43].

VII. CONCLUSION

In summary, we have developed the first NHP-MPI, characterized by a bore size of 190 mm. Through a digital-scanned focus field, 3-D imaging with an FOV of 120 × 120 × 120 mm^3 can be obtained. Comprehensive performance evaluations of the system were conducted in the article, which demonstrated that our system has a detection limit of 19.53 μg_{Fe}, with sensitivity uniformity over the FOV. Besides, our system achieves the spatial resolution of 8, 16, and 8 mm in the (x, y, z) axes, respectively. Furthermore, the system showed good quantitative performance in brain imaging experiments on macaque subjects, which demonstrated the further possibilities for exploring application on the brain diseases such as stroke, particularly, cerebral hemorrhage.

APPENDIX

Here, we introduce the generation of FFP in our system. Here, we consider ideal magnetic fields. First, the FFP is created using a linear gradient magnetic field denoted as the selection field $\boldsymbol{H}^{\mathrm{S}}(\boldsymbol{r})$. Subsequently, a drive field $H^{\mathrm{D}}(t)$, characterized by a homogeneous alternating magnetic field, is applied to excite the SPIO to produce a nonlinear magnetization response, with the drive field oriented along the borehole direction (x-direction). In this study, a 3-D focus field sequence is employed to move the FFP to scan the entire 3-D FOV. Rather than creating an FOV, the drive field is regarded as an excitation field which is used to excite the particle signal. The 3-D focus field $\boldsymbol{H}^{\mathrm{F}}(t)$ consists of three homogeneous magnetic fields that are orthogonal to each other and generated according to a given time sequence. The total magnetic field $\boldsymbol{H}(\boldsymbol{r}, t)$ can be described as

$$\boldsymbol{H}(\boldsymbol{r}, t) = \boldsymbol{H}^{S}(\boldsymbol{r}) + H^{D}(t)\boldsymbol{e}_x + \boldsymbol{H}^{F}(t) \tag{9}$$

with

$$\boldsymbol{H}^{S}(\boldsymbol{r}) = G_x x\boldsymbol{e}_x + G_y y\boldsymbol{e}_y + G_z z\boldsymbol{e}_z \tag{10}$$

$$H^{D}(t) = A^{D}\cos\left(2\pi f^{D} t\right) \tag{11}$$

where $\boldsymbol{r} = [x, y, z]^T$, and G_x, G_y, and G_z represent the field gradient in the (x, y, z) directions, respectively. $G_z = -2G_y = -2G_x$. f^D and A^D denote the frequency and amplitude of the drive field, respectively.

ACKNOWLEDGMENT

The authors would like to acknowledge the instrumental and technical support of Multimodal Biomedical Imaging Experimental Platform, Institute of Automation, Chinese Academy of Sciences, and the National Research Facility for Phenotypic and Genetic Analysis of Model Animals (Primate Facility). They are also thankful to Prof. Yonggang Yao and Prof. Bingyu Mao for their valuable suggestions and discussions.

REFERENCES

[1] B. Gleich and J. Weizenecker, "Tomographic imaging using the nonlinear response of magnetic particles," *Nature*, vol. 435, no. 7046, pp. 1214–1217, Jun. 2005.

[2] W. Tong et al., "Sensitive magnetic particle imaging of haemoglobin degradation for the detection and monitoring of intraplaque haemorrhage in atherosclerosis," *eBioMedicine*, vol. 90, Apr. 2023, Art. no. 104509.

[3] J. Zhuo et al., "Enhanced glypican-3-targeted identification of hepatocellular carcinoma with liver fibrosis by pre-degrading excess fibrotic collagen," *Acta Biomaterialia*, vol. 158, pp. 435–448, Mar. 2023.

[4] M. P. Bui, T.-A. Le, and J. Yoon, "A magnetic particle imaging-based navigation platform for magnetic nanoparticles using interactive manipulation of a virtual field free point to ensure targeted drug delivery," *IEEE Trans. Ind. Electron.*, vol. 68, no. 12, pp. 12493–12503, Dec. 2021.

[5] J. Rahmer, D. Wirtz, C. Bontus, J. Borgert, and B. Gleich, "Interactive magnetic catheter steering with 3-D real-time feedback using multi-color magnetic particle imaging," *IEEE Trans. Med. Imag.*, vol. 36, no. 7, pp. 1449–1456, Jul. 2017.

[6] X. Huang et al., "Deep penetrating and sensitive targeted magnetic particle imaging and photothermal therapy of early-stage glioblastoma based on a biomimetic nanoplatform," *Adv. Sci.*, vol. 10, no. 19, Jul. 2023, Art. no. 2300854.

[7] T. Zhu et al., "Accurate concentration recovery for quantitative magnetic particle imaging reconstruction via nonconvex regularization," *IEEE Trans. Med. Imag.*, early access, Apr. 1, 2024, doi: 10.1109/TMI.2024.3383468.

[8] L. Yin et al., "Recent developments of the reconstruction in magnetic particle imaging," *Vis. Comput. for Ind., Biomed., Art*, vol. 5, no. 1, Oct. 2022, Art. no. 24.

[9] P. Szwargulski et al., "Monitoring intracranial cerebral hemorrhage using multicontrast real-time magnetic particle imaging," *ACS Nano*, vol. 14, no. 10, pp. 13913–13923, Oct. 2020.

[10] W. Tong et al., "Highly sensitive magnetic particle imaging of vulnerable atherosclerotic plaque with active myeloperoxidase-targeted nanoparticles," *Theranostics*, vol. 11, no. 2, pp. 506–521, 2021.

[11] B. Gleich, J. Weizenecker, and J. Borgert, "Experimental results on fast 2D-encoded magnetic particle imaging," *Phys. Med. Biol.*, vol. 53, no. 6, pp. N81–N84, Mar. 2008.

[12] J. Weizenecker, B. Gleich, J. Rahmer, H. Dahnke, and J. Borgert, "Three-dimensional real-timein vivomagnetic particle imaging," *Phys. Med. Biol.*, vol. 54, no. 5, pp. L1–L10, Mar. 2009.

[13] M. Graeser et al., "Towards picogram detection of superparamagnetic iron-oxide particles using a gradiometric receive coil," *Sci. Rep.*, vol. 7, no. 1, Jul. 2017, Art. no. 6872.

[14] Z. W. Tay et al., "Pulsed excitation in magnetic particle imaging," *IEEE Trans. Med. Imag.*, vol. 38, no. 10, pp. 2389–2399, Oct. 2019.

[15] F. Mohn, T. Knopp, M. Boberg, F. Thieben, P. Szwargulski, and M. Graeser, "System matrix based reconstruction for pulsed sequences in magnetic particle imaging," *IEEE Trans. Med. Imag.*, vol. 41, no. 7, pp. 1862–1873, Jul. 2022.

[16] T. Knopp, N. Gdaniec, and M. Möddel, "Magnetic particle imaging: From proof of principle to preclinical applications," *Phys. Med. Biol.*, vol. 62, no. 14, pp. R124–R178, Jun. 2017.

[17] K. Gräfe, A. von Gladiss, G. Bringout, M. Ahlborg, and T. M. Buzug, "2D images recorded with a single-sided magnetic particle imaging scanner," *IEEE Trans. Med. Imag.*, vol. 35, no. 4, pp. 1056–1065, Apr. 2016.

[18] P. W. Goodwill, J. J. Konkle, B. Zheng, E. U. Saritas, and S. M. Conolly, "Projection X-space magnetic particle imaging," *IEEE Trans. Med. Imag.*, vol. 31, no. 5, pp. 1076–1085, May 2012.

[19] J. Franke et al., "System characterization of a highly integrated preclinical hybrid MPI-MRI scanner," *IEEE Trans. Med. Imag.*, vol. 35, no. 9, pp. 1993–2004, Sep. 2016.

[20] C. B. Top and A. Güngör, "Tomographic field free line magnetic particle imaging with an open-sided scanner configuration," *IEEE Trans. Med. Imag.*, vol. 39, no. 12, pp. 4164–4173, Dec. 2020.

[21] J. W. M. Bulte, "Superparamagnetic iron oxides as MPI tracers: A primer and review of early applications," *Adv. Drug Del. Rev.*, vol. 138, pp. 293–301, Jan. 2019.

[22] T.-A. Le, M. P. Bui, and J. Yoon, "Development of small-rabbit-scale three-dimensional magnetic particle imaging system with amplitude-modulation-based reconstruction," *IEEE Trans. Ind. Electron.*, vol. 70, no. 3, pp. 3167–3177, Mar. 2023.

[23] M. Graeser et al., "Human-sized magnetic particle imaging for brain applications," *Nature Commun.*, vol. 10, no. 1, Apr. 2019, Art. no. 1936.

[24] M. P. B. T.-A. Le, K. M. Gadelmowla, S. Oh, and J. Yoon, "First human-scale magnetic particle imaging system with superconductor," *Int. J. Magn. Part. Imag.*, vol. 9, no. 1, 2023, Art. no. 2303032.

[25] H. Hui et al., "In vivo measurement of cerebral SPIO concentration in nonhuman primate using magnetic particle imaging detector," *IEEE Magn. Lett.*, vol. 14, pp. 1–5, 2023.

[26] S. Shirmohammadi and A. Ferrero, "Camera as the instrument: The rising trend of vision based measurement," *IEEE Instrum. Meas. Mag.*, vol. 17, no. 3, pp. 41–47, Jun. 2014.

[27] P. Vogel, M. A. Rückert, P. Klauer, W. H. Kullmann, P. M. Jakob, and V. C. Behr, "Traveling wave magnetic particle imaging," *IEEE Trans. Med. Imag.*, vol. 33, no. 2, pp. 400–407, Feb. 2014.

[28] P. W. Goodwill and S. M. Conolly, "The X-space formulation of the magnetic particle imaging process: 1-D signal, resolution, bandwidth, SNR, SAR, and magnetostimulation," *IEEE Trans. Med. Imag.*, vol. 29, no. 11, pp. 1851–1859, Nov. 2010.

[29] Y. Liu et al., "Weighted sum of harmonic signals for direct imaging in magnetic particle imaging," *Phys. Med. Biol.*, vol. 68, no. 1, Jan. 2023, Art. no. 015018.

[30] A. A. Ozaslan, M. Utkur, U. Canpolat, M. A. Tuncer, K. K. Oguz, and E. U. Saritas, "PNS limits for human head-size MPI systems: Preliminary results," *Int. J. Magn. Part. Imag.*, vol. 8, no. 1, 2022, Art. no. 2203028.

[31] D. J. Schaefer, J. D. Bourland, and J. A. Nyenhuis, "Review of patient safety in time-varying gradient fields," *J. Magn. Reson. Imag.*, vol. 12, no. 1, pp. 20–29, Jul. 2000.

[32] H. Zhang, S. Japee, A. Stacy, M. Flessert, and L. G. Ungerleider, "Anterior superior temporal sulcus is specialized for non-rigid facial motion in both monkeys and humans," *NeuroImage*, vol. 218, Sep. 2020, Art. no. 116878.

[33] C. Z. Cooley, J. B. Mandeville, E. E. Mason, E. T. Mandeville, and L. L. Wald, "Rodent cerebral blood volume (CBV) changes during hypercapnia observed using magnetic particle imaging (MPI) detection," *NeuroImage*, vol. 178, pp. 713–720, Sep. 2018.

[34] M. Meribout and M. Kalra, "A portable system for two dimensional magnetic particle imaging," *Measurement*, vol. 152, Feb. 2020, Art. no. 107281.

[35] T. Zhu, J. He, Z. Wei, H. Hui, X. Yang, and J. Tian, "A design of a low-power open-side MPI scanner Using inverted spliced permanent magnets," *Int. J. Magn. Part. Imag.*, vol. 9, no. 1, 2023, Art. no. 2303072.

[36] G. Jia et al., "Gradient-based pulsed excitation and relaxation encoding in magnetic particle imaging," *IEEE Trans. Med. Imag.*, vol. 41, no. 12, pp. 3725–3733, Dec. 2022.

[37] Y. Li et al., "Modified Jiles–Atherton model for dynamic magnetization in X-space magnetic particle imaging," *IEEE Trans. Biomed. Eng.*, vol. 70, no. 7, pp. 2035–2045, Dec. 2023.

[38] Y. Shang et al., "Deep learning for improving the spatial resolution of magnetic particle imaging," *Phys. Med. Biol.*, vol. 67, no. 12, Jun. 2022, Art. no. 125012.

[39] J. Zhang, Z. Wei, X. Wu, Y. Shang, J. Tian, and H. Hui, "Magnetic particle imaging deblurring with dual contrastive learning and adversarial framework," *Comput. Biol. Med.*, vol. 165, Oct. 2023, Art. no. 107461.

[40] G. Shi et al., "Progressive pretraining network for 3D system matrix calibration in magnetic particle imaging," *IEEE Trans. Med. Imag.*, vol. 42, no. 12, pp. 3639–3650, Dec. 2023.

[41] H. Peng et al., "Multi-scale dual domain network for nonlinear magnetization signal filtering in magnetic particle imaging," *Biomed. Signal Process. Control*, vol. 85, Aug. 2023, Art. no. 104863.

[42] Z. Wei, Y. Liu, T. Zhu, X. Yang, J. Tian, and H. Hui, "BSS-TFNet: Attention-enhanced background signal suppression network for time-frequency spectrum in magnetic particle imaging," *IEEE Trans. Emerg. Topics Comput. Intell.*, vol. 8, no. 2, pp. 1322–1336, Apr. 2024.

[43] E. E. Mason et al., "Functional magnetic particle imaging (fMPI) of cerebrovascular changes in the rat brain during hypercapnia," *Phys. Med. Biol.*, vol. 68, no. 17, Sep. 2023, Art. no. 175032.